THESIS FOR THE DEGREE OF LICENTIATE OF ENGINEERING

Towards Microwave Detection of Thromboses

Seyed Moein Pishnamaz

CHALMERS
UNIVERSITY OF TECHNOLOGY

Department of Electrical Engineering
Chalmers University of Technology
Gothenburg, Sweden, 2022

Towards Microwave Detection of Thromboses

Seyed Moein Pishnamaz

Technical Report No.
ISSN
This thesis has been prepared using LaTeX.

Department of Electrical Engineering
Chalmers University of Technology
SE-412 96 Gothenburg, Sweden
Phone: +46 (0)31 772 1000
www.chalmers.se

Printed by Chalmers Reproservice
Gothenburg, Sweden, December2022

Abstract

Stroke is estimated to be the second most common cause of death with huge burdens and costs for the patient and society. Since the treatment given to a stroke patient depends on the type of stroke they have, a fast and reliable diagnosis of the stroke type is needed before any treatment can be started. In general, the treatment is more effective the sooner it is started. Thrombectomy is an interventional treatment for patients with an occlusion (thrombosis) in a large artery that is only performed in a limited number of hospitals, thus early detection can support the pre-hospital decision-making process and help decreasing the time to treatment start. The aim of this work is to investigate and develop a method for pre-hospital diagnosis of ischemic stroke by using a microwave diagnosis setup and Contrast-Enhancement Agent (CEA). We propose to exploit the asymmetry created in the brain as a result of partial or full blockage of the arteries due to thromboses. This asymmetry is enhanced with the use of CEA and can be captured by the EM waves transmitted and received by the antennas on the head.

The microwave diagnosis setup consists of several antennas placed on the body. The multipath interference caused by the waves traveling on the surface of the body is a factor that limits the detection accuracy of this system. In the present study, a Dielectric Rod Antenna (DRA) is designed to address this challenge with a Self Grounded Bow-Tie Antenna (SGBTA) as the wave exciter. It was shown that DRA can reduce the surface wave power up to 10 dB in comparison with that of SGBTA while increasing its bandwidth by 72

Preliminary results obtained from measurements on sheep show are promising.

Keywords: Stroke, Thromboses, Microwave, Antenna.

List of Publications

This thesis is based on the following publications:

[A] **Seyed Moein Pishnamaz, Xuezhi Zeng, Hana Dobšíček Trefná, Mikael Persson, Andreas Fhager**, "Minimising the Surface Waves By Using a Dielectric Rod Antenna in Near-Field Biomedical Diagnostics". To be Submitted to IEEE Transactions on Antenna and Propagation.

[B] **Seyed Moein Pishanamz**, Andreas Fhager, Mikael Persson, "Analysis of the 2D Guided Mode Propagation in a 3D Dielectric Rod Antenna". Submitted to 17th European Conference on Antenna and Propagation.

Other publications by the author, not included in this thesis, are:

[C] **Seyed Moein Pishnamaz**, Andreas Fhager, Mikael Persson, "Microwave Detection of The Shunt Malfunction in Hydrocephalus Children". *ESHO2022*, 34th Annual Meeting European Society for Hyperthermic Oncology, 14–17 September 2022, Gothenburg .

[D] **Seyed Moein Pishnamaz**, Andreas Fhager, Mikael Persson, "Microwave Detection of The Shunt Malfunction in Hydrocephalus Children". *Medicinteknikdagarna* , 4-6 Oktober 2022, Luleå.

Acknowledgments

I would like to thank Prof. Mikael Persson, for giving me the opportunity to continue my studies under his supervision as a PhD student. I appreciate his holistic approach and attentive criticisms. I would like to express my gratitude towards Associate Prof. Andreas Fhager and Dr. Xuezhi Zeng, my co-supervisors, for all the help they provided during these years and especially during writing this thesis. My appreciation goes to Associate Prof. Hana Dobsicek Trefna for our antenna discussions and for helping out during measurement campaigns.

I had the great opportunity of turning colleagues into friends who were by my side in the ups and downs. Thank you, Laura and Mattia for your support, helping out in the lab and office and after-works. I would like to thank my friends Dmitrii, Chouaib, Asta & Mauricio, Anna, Alvin, August, and former colleagues Samar, Morteza, and Karan.

I would like to thank the "Persian Couples" network that is formed around us. You make here like home: Mohammad & Neda, Niloofar & Navid, Nima & Marziyeh, Mostafa & Zahra, Hadi & Samin, Fredows & Saeed, and Reza & Afsaneh.

Speaking of home, I should appreciate my family back there for supporting me, my father and father-in-law, my mother and mother-in-law, and my brother Amin.

Last but not least, I would like to thank Shokoofeh. During this journey, we evolved from friends to lovers, and from lovers to husband and wife. Thank you for all your patience, sacrifice, love, and the meaning you give to my life.

Moein, December 2022, Gothenburg

Acronyms

DRA:	Dielectric Rod Antenna
SGBTA:	Self-Grounded Bow-tie Antenna
CEA:	Contrast-Enhancing Agent

Contents

Part I

Overview

CHAPTER 1

Introduction

Stroke is a condition in which, blood flow to the brain is deficient. There are two main types of stroke: Ischemic and hemorrhagic. While in the former type, an occlusion prevents the blood to flow, in the latter case, bleeding has occurred in the brain due to a ruptured vessel as shown in Fig. 1.1. Both types of stroke are frequent around the world. In Fig. 1.2, the 2019 age-standardized stroke incidence rates per 100000 people are shown for different countries, first for all stroke types and then based on the type of stroke. Following the pattern of the shades of red colour in Fig. 1.2 the ischemic type is the most common type.

Stroke is estimated to be the second most common cause of death [3] and the third most common cause of disability-adjusted life years (DALYs) [4]. One DALY represents the loss of the equivalent of one year of full health and is considered to be a good measure of the burden of stroke [5]. Stroke is not only widespread but also costly. The total 2010 European cost has been estimated to be €64.1 billion [6]. The mean US lifetime cost of an ischemic stroke patient has been estimated to be around $140,000 [7].

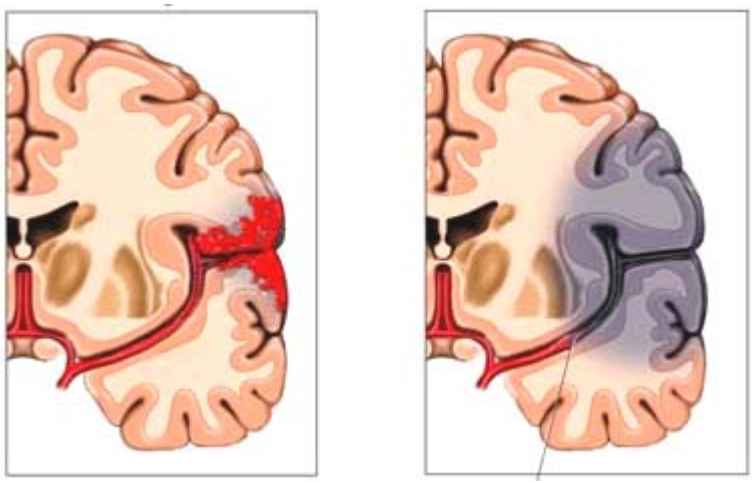

Figure 1.1: Stroke Types. Left Hemorrhagic and right Ischemic. The red area on the left shows the bleeding and the grey area in right shows the deoxygenated brain tissue. [1]

1.1 Background

In this section, we will take a glance at the medical diagnosis and treatment of stroke. As it was mentioned before, ischemic stroke is when an artery is blocked by thrombosis i.e. a clot. Thrombolysis is one of the most common treatments given to patients with ischemic stroke [8] with the aim to dissolve the thromboses. Another effective treatment for patients diagnosed with thrombosis in the bigger arteries is Thrombectomy. This is an interventional procedure [9] where the thrombosis is removed mechanically by inserting a catheter into the cerebral arteries. Thrombectomy is most effective if it is done early, preferably, at least within 3 to 4.5 hours after the onset of symptoms [10].

Treatments for hemorrhagic stroke (bleeding) and ischemic stroke (clot) are quite different. While thrombolysis can save the life of a patient with an ischemic stroke, performing the same treatment on a hemorrhagic patient can have fatal consequences. Therefore, the correct early diagnosis of the type of stroke is vital. Furthermore, only a few specialist hospitals are able to perform Thrombectomy. For example in the Västra-Götaland region in Sweden, only

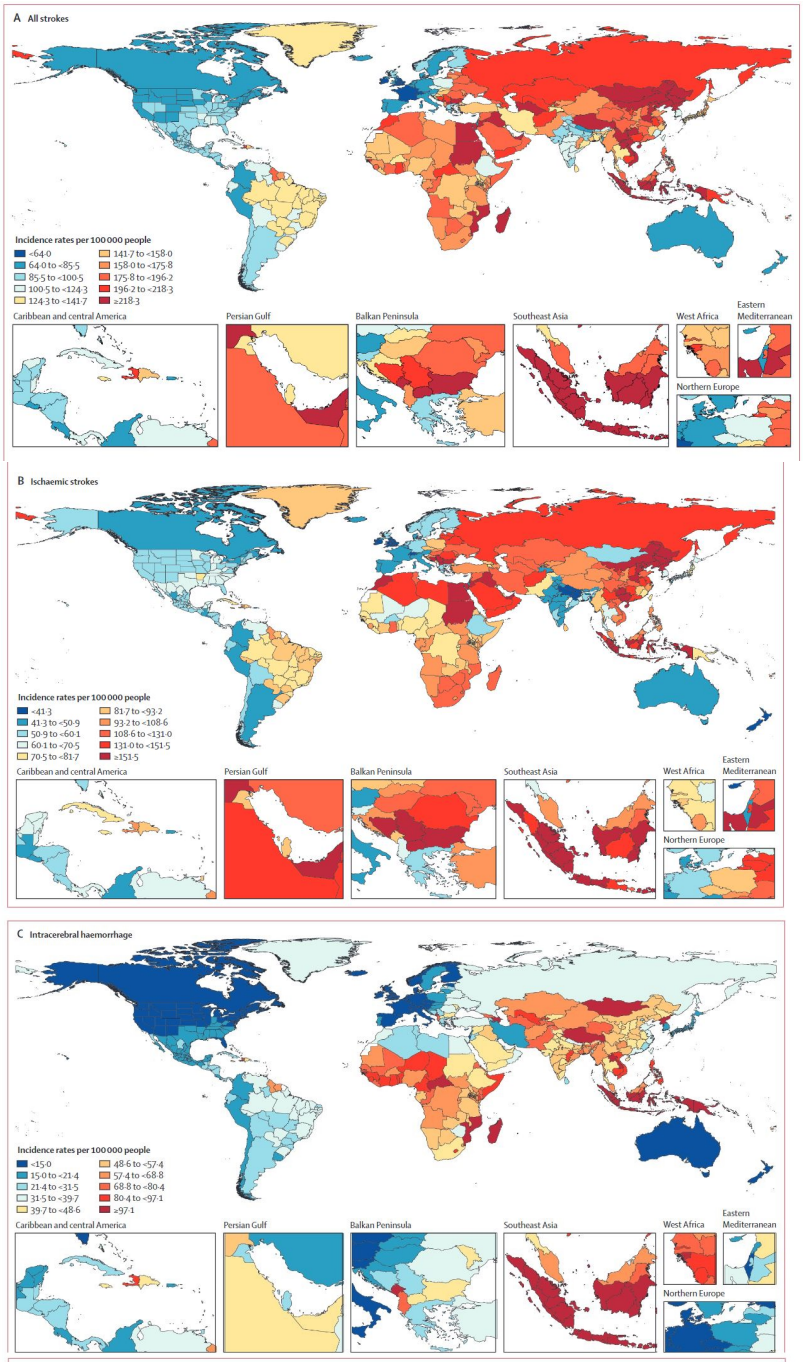

Figure 1.2: Age-standardised stroke incidence rates per 100000 people by stroke type and country, for both sexes, 2019(A) All strokes. (B) Ischaemic stroke. (C) Intracerebral haemorrhage [2]

Sahlgrenska University hospital accepts patients for Thrombectomy [11]. In a recent study, it was shown that five times more patients could have been treated with thrombectomy than are treated today [11]. If a fast and reliable diagnosis could be made in the ambulance so that the right patient could be delivered to the right hospital faster.

Currently, one common practice to assess patients in order to identify candidates for thrombectomy in the ambulance is to use a clinical evaluation tool called Modified NIH Stroke Scale/Score (mNIHSS). This scale shows the severity of the stroke based on clinical observations of the patient. The fact that it only relies on observations, not measurements, suggests that adding objective measurements could complement and improve the triage of the patients.

Microwave diagnostics has been shown to be a compliment to other diagnostic modalities [12]–[15]. As the microwave is non-ionizing it can be an alternative to ionized X-rays used in Computed Tomography (CT). This research has been enabled by recent development in microwave technology, mainly due to the demands of the telecommunication industry. Therefore, there today exists microwave technology that are fast in operation, small in size, and cost-efficient [16]. There are other diagnostic modalities in the area of pre-hospital stroke detection such as bioelectrical impedance [17] and near-infrared spectroscopy [18]. The advantage of microwave diagnosis over the two mentioned methods is the ability to detect both superficial and deep targets [19]. In a recent bibliometric analysis, it was shown that microwave imaging is among the top 3 studied modalities for pre-hospital stroke detection devices [13]. In the next section, the principles of microwave diagnostics and some examples of the methods are presented.

In the next two sections, the words used in the title of this thesis are explained and the connection between them is introduced. This is done first by defining the term ”microwave” and then introducing ”microwave diagnosis of stroke”.

1.2 Electromagnetic Waves

In this section, an introduction to Electromagnetic (EM) waves is presented.

The propagation of EM waves is governed by Maxwell’s equations [20]. Maxwell’s equation for the time-harmonic fields in the phasor notation is as

follows:

$$\nabla \cdot \bar{\mathbf{D}} = \rho \quad \text{Gauss's Law} \tag{1.1}$$
$$\nabla \cdot \bar{\mathbf{B}} = 0 \quad \text{Gauss's Law for Magnetism} \tag{1.2}$$
$$\nabla \times \bar{\mathbf{E}} = -j\omega\bar{\mathbf{B}} \quad \text{Faraday's Law of Induction} \tag{1.3}$$
$$\nabla \times \bar{\mathbf{H}} = j\omega\bar{\mathbf{D}} + \bar{J} \quad \text{Ampere's Circuital Law} \tag{1.4}$$

where $\bar{\mathbf{D}}$ and $\bar{\mathbf{B}}$ are electric and magnetic flux density and $\bar{\mathbf{E}}$ and $\bar{\mathbf{H}}$ are the electric and magnetic field intensity respectively. volume charge density is shown by ρ and Surface current density $\bar{J}$ is the sum of source currents $\bar{J}_i$ and currents created because of the conduction in the material, $\bar{J}_c$ which in the linear case is related to the electric field by the conductivity of the material σ:

$$\bar{J}_c = \sigma\bar{\mathbf{E}} \tag{1.5}$$

The relation between the flux density and the field intensity for a linear homogeneous isotropic material is as follows:

$$\bar{\mathbf{D}} = \epsilon_0\epsilon_r\bar{\mathbf{E}} \tag{1.6}$$
$$\bar{\mathbf{B}} = \mu_0\mu_r\bar{\mathbf{H}} \tag{1.7}$$

ϵ_0 and μ_0 are the permittivity and permeability of the vacuum respectively. ϵ_r and μ_r are the relative permittivity and relative permeability of the material where the EM wave is propagating. In a source-free, $\rho = 0$, $\bar{J}_i = 0$, and nonmagnetic $\mu_r = 1$ medium Maxwell's equations reduce to:

$$\nabla \cdot \bar{\mathbf{E}} = 0 \tag{1.8}$$
$$\nabla \cdot \bar{\mathbf{H}} = 0 \tag{1.9}$$
$$\nabla \times \bar{\mathbf{E}} = -j\omega\mu_0\bar{\mathbf{H}} \tag{1.10}$$
$$\nabla \times \bar{\mathbf{H}} = j\omega\epsilon_0\epsilon_{rc}\bar{\mathbf{E}} \tag{1.11}$$

Where ϵ_{rc} is the complex relative permittivity of the medium and is defined as:

$$\epsilon_{rc} = \epsilon_r + \frac{\sigma}{j\omega\epsilon_0}. \tag{1.12}$$

Taking $\nabla\times$ from both sides of (1.10) and substituting in (1.11) results in

the following equation:

$$\nabla \times \nabla \times \bar{\mathbf{E}} \quad = \quad \gamma^2 \bar{\mathbf{E}} \tag{1.13}$$

Where $\gamma^2 = \omega^2 \mu_0 \epsilon_0 \epsilon_{rc}$. The left-hand side of the equation can be re-written as:

$$\nabla \cdot (\nabla \cdot \bar{\mathbf{E}}) - \nabla^2 \bar{\mathbf{E}} \quad = \quad \gamma^2 \bar{\mathbf{E}} \tag{1.14}$$

From (1.8), the first expression in (1.14), becomes zero. Therefore, (1.14) results in the following equation which is called the wave equation:

$$\nabla^2 \bar{\mathbf{E}} \quad + \quad \gamma^2 \bar{\mathbf{E}} \quad = \quad 0 \tag{1.15}$$

The most simple solution to the wave equation is a 1-dimensional plane wave propagating in the z-direction.

$$\bar{\mathbf{E}} = (E_{x0}\hat{x} + E_{y0}\hat{y})e^{-j\gamma z} \tag{1.16}$$

γ can also be written as $\gamma = \beta - j\alpha$. In this case, β is the wave number and α is the attenuation constant in the lossy material.

The wave propagating in a lossy media will lose power. This power is absorbed in the material and dissipated as heat. Yet another effect of the media on the propagation of the EM wave occurs when there is a discontinuity i.e. a change in the spatial distribution of the permittivity and conductivity of the media. Two phenomena that occur when at such a boundary are reflection and transmission as shown in Fig. 1.3. The EM wave in a multi-layer environment like the human body experiences multiple reflections and transmissions each of which changes its magnitude and phase. These changes can be sensed by a sensor i.e. an antenna, and further analyzed by proper signal processing algorithms. This makes the foundation of every electromagnetic-based diagnosis method.

Microwaves are a type of EM wave that corresponds to frequencies from 300 MHz to 300 GHz as shown in Fig. 1.4. the lower band of this range is shown to be more practical for biomedical applications since the attenuation of the waves in the biological tissues like the human body is lower in comparison with higher frequencies [21].

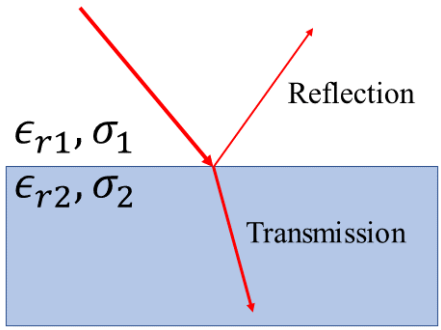

Figure 1.3: Interactions of the EM Waves with Materials

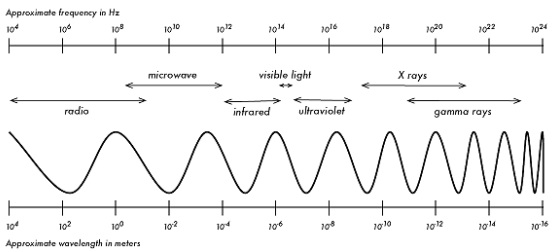

Figure 1.4: Electromagnetic Spectrum [22]

1.3 Microwave Diagnosis of Stroke

In a generic microwave diagnosis system, as shown in Fig. 1.5, several antennas, shown by blue circles, operating in microwave frequencies are placed around the body, shown as a multi-layer ellipse. The antennas could in principle be operated in many different schemes, such as mono-static, bi-static, or multi-static. In this work, we use a multi-static scheme, where one antenna transmits an EM wave at a time while others receive. Then, the transmitting antenna is changed until all the antennas have transmitted once. Measured data is collected in form of scattering parameters [23]. The scattering parameters show the amount of change that occurred in the magnitude and phase of the transmitted wave when it passed through the medium. Therefore, it bears information about the dielectric distribution of the medium.

It has been shown that several changes related to diseases and traumas in the human body result in a change in the EM characteristics of the corresponding tissue. Therefore, these changes can be sensed by EM waves.

Other application areas where a dielectric contrast between healthy and non-healthy tissue can be utilized for diagnostic purposes include microwave imaging of breast tumors [24], [25], muscle quality [26], muscle rupture [27] and steatotic liver detection [28].

One such diagnostic scenario is stroke as shown in Fig. 1.6. For hemorrhagic stroke as the permittivity of the blood pool created in the brain is different from the brain tissue, EM detection is possible [29]. Extensive efforts in this area had been done by the group at the Chalmers University of Technology [12], [30], [31]. Several generations of a Stroke finder device have been developed and the current generation, shown in Fig. 1.7, is CE marked and ready to be used in supporting pre-hospital decision-making [15]. There are some other groups worldwide who are pursuing the same topic and have attained promising results [32]–[34].

For ischemic stroke, the blood clots blocking the vessels are so small that the effect caused by the change in the permittivity that they create is subtle and could be easily drowned in the noise or interference from the environment. On the other hand, the lack of blood in the infarction area can result in a change in the permittivity [36]. There had been some research studies mainly on simulated data and phantom measurements towards microwave diagnosis of ischemic stroke [37], [38].

The key challenge here is to differentiate between small vessel occlusions

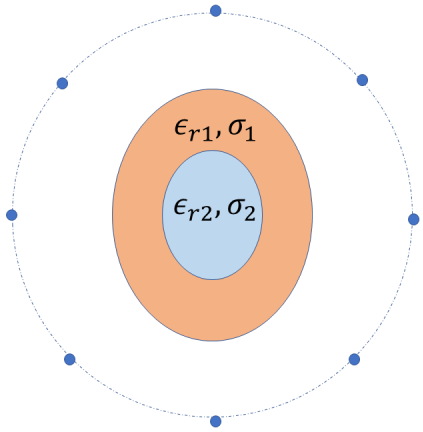

Figure 1.5: A Generic Microwave Diagnosis System [12]

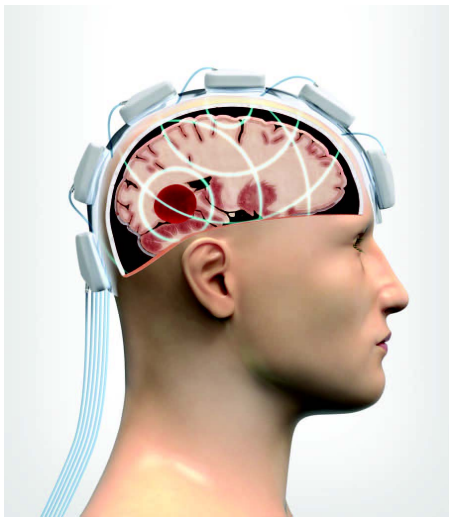

Figure 1.6: A Microwave-based Stoke Diagnosis System [12]

Figure 1.7: MD100 Device developed by Medfield Diagnostics AB [30], [35]

that are treated with thrombolysis and the large vessel occlusions that are candidates for thrombectomy. A way to enhance the contrast between the area of the infraction and healthy tissue is to use Contrast-Enhancing Agents (CEAs). Using CEAs in other imaging modalities like MRI is common and dates back to decades ago [39]. Various CEAs have been used in microwave diagnostics including iron nanoparticles [40], Zinc oxide nanoparticles [41], Superparamagnetic Iron Oxide Nanoparticles [42], and Saline [43]. The use of nanoparticles in connection with microwave measurements has been tested on rabbits [40].

In the present work, we propose to exploit the asymmetry created in the brain as a result of partial or full blockage of the arteries due to thromboses. This asymmetry is enhanced with the use of CEA as it is injected venously and then transported to the brain through the arteries after passing through the heart and lungs. In the brain, it is distributed unevenly as a result of the blocked arteries. The artery that is blocked by the thrombus, makes the distribution of the contrast agent uneven in the brain. This change in the dielectric property of the region with and without the CEA can be captured by the EM waves transmitted and received by the antennas on the body.

As mentioned earlier, it is desired to operate in lower frequencies to ensure enough penetration of the wave to internal organs [21]. On the other hand, the antennas operating at low frequencies are physically large and challenging to fit around the body. In this research, the radiating element of the antenna is

immersed inside a medium with high relative permittivity to make the antenna physically small and to keep its electrical size constant [44]–[47].

A typical drawback of a microwave-based diagnosis system with several antennas around the body is mutual coupling through surface waves. The wave that is intended to penetrate through the body and received by the other antenna in the direct path travels around the body [48]. These will be received by the adjacent antennas and interfere with the direct-path wave [49]. This path deteriorates the diagnosis accuracy as it does not contain information from the areas of interest and is more sensitive to environmental changes.

In this work, we present a solution to minimize surface waves by moving the radiating element of the antenna at a distance from the surface of the body and placing a dielectric rod in between. It is shown that the power is confined inside the rod toward the body rather than propagating on its surface while the antenna is still matched to the body. The matching of the antenna to the body is important since it enables ultra-wideband operation which can improve the resolution of the diagnostics [50].

1.4 Aim of the Study and Thesis outline

The aim of this study is to investigate the possibility of a pre-hospital diagnosis of ischemic stroke by using a microwave diagnosis setup and contrast-enhancement agent. Another aim is to test it in an animal study. For this study, a wide-band low-interference body-matched antenna is designed. The design is explained thoroughly in paper A. In chapter 2, supplementary materials to the antenna design are given. In chapter 3, a report on the planned animal study is given. Some preliminary results of an unsupervised anomaly detection algorithm on the measured data of a previous animal study are also presented. Another aim is to develop this algorithm. Chapter 4 presents a summary of the appended papers. The conclusion of the first part of the thesis is given in chapter 5.

CHAPTER 2

Antenna Design

Several factors need to be considered in designing an antenna for biomedical diagnostics applications. To list a few:

- **Bandwidth:** The bandwidth of an antenna is characterized by the range of the frequencies where the reflection coefficient of the antenna falls below -10 dB. In this work, the goal is to have an ultra-wideband antenna that can operate at a large range of frequencies that enables high-resolution diagnostics [51].
- **Deep Penetration into the Tissue:** As the attenuation of the microwaves inside a lossy environment like biological tissues increases with the frequency of the signal, it is desired to operate in lower frequencies to ensure enough penetration of the wave to internal organs [21].
- **Compactness:** In a microwave-based biomedical diagnosis system several antennas are commonly placed around the body [52], [53]. Therefore, the antenna's physical size should be small enough.
- **Interference Susceptibility:** One problem of on-body antennas is the existence of surface or creeping waves [48]. A part of the radiated wave

travels on the surface of the body and is then received by the adjacent antennas, interfering with the direct-path wave and deteriorating the diagnosis accuracy [49]. Therefore, the goal is to mitigate this multi-path signal.

It's challenging to design an antenna that possesses all the above-mentioned features as attaining one can result in losing the other. For example, an antenna that operates at low frequencies is physically large, therefore it hinders compactness. Additionally, reaching a wide bandwidth at low frequencies is challenging [54].

To overcome the aforementioned challenges and meet the goals, a Dielectric Rod Antenna (DRA) is proposed. The antenna is composed of a radiating element, a Self-Grounded Bow-Tie Antenna (SGBTA), and a two-layer dielectric rod. The idea behind this antenna design is to move away the radiating element and guide the radiated wave toward the body by using the dielectric rod, so the surface wave is minimized. It is shown that the proposed new antenna design gives a wider bandwidth, stable near-field gain, and a more confined distribution of the power on the surface of the body. The design of this antenna is explained in detail in the following section and paper A in the appendix.

2.1 Dielectric Rod Antenna Design

In this section, the design of the DRA is introduced. This design begins with a 2-dimensional analytical solution to the wave propagation problem in a 2-layers cylindrical structure as shown in Fig. 2.1. This structure consists of a cylindrical core (blue) and cladding (gray) and is aligned with the z-axis. Parameters a and b are the radii and ϵ_{r1} and ϵ_{r2} are the relative permittivities of the core and the cladding respectively. In this analysis, we consider lossless materials with $\epsilon_{r1} = 80$ and $\epsilon_{r2} = 2$ which are close to the permittivity of water and plastic respectively. The surrounding medium is considered to be vacuum $\epsilon_{r3} = 1$. It has been stated in [55], to only excite the fundamental mode of the DRA, the radius of the DRA should satisfy the following condition: $2a < \frac{0.626}{\sqrt{\epsilon_{r1}}}\lambda_0$ where λ_0 is the wavelength in vacuum. Considering 700 MHz which is among the frequency range of interest and $\epsilon_r = 80$, a should be smaller than 1.5 cm. On the other hand, to have the field confined to the core, the diameter should be larger than $\frac{\lambda_0}{4}$ [55], resulting in $a > 5.3$ cm. This is in

contradiction with the first condition on a and the rule of thumb conditions that were mainly derived for antennas operating at higher frequencies can not be simply applied here. Instead, a more precise study is needed to evaluate the mode of excitation and field confinement in DRA in order to come up with a proper design. Therefore, an analytical solution to the wave propagation in an infinite 2D cylindrical structure is presented with emphasis putting on the radius of the core of the dielectric rod as it plays an essential role in the wave propagation in this structure. The field is not confined to the surface of the rod if the core radius is too small while a larger core radius may lead to the excitation of higher, unwanted modes. As a compromise, the value of the core radius is chosen in a way that the fields are confined in the rod and a higher-order mode is excited. Then a mode suppressor is designed to suppress that mode. Finally, numerical 3D simulations and experimental measurements confirm the design in paper A. The connection between the 2D analysis and 3D numerical simulations is investigated in paper B.

Analytical Solution for a 2 layers DRA

The first step of the dielectric rod antenna design is to understand the mechanisms of wave propagation in this structure. In this section, the wave propagation problem in a 2-dimensional cylindrical structure as shown in Fig. 2.1 is studied.

In [56], an analytical solution to the wave propagation problem in this structure is presented. According to the separation of variable technique [57], the solutions to the homogeneous wave equation are found and called the modes of the structure. The axial component of the electric and magnetic fields of these modes can be written as follows [56]:

$$\begin{aligned} E_{z1} &= A_{n1} Z_{n1}(k_1 r) P_n \quad 0 \le r \le a \\ H_{z1} &= B_{n1} Z_{n1}(k_1 r) Q_n \quad 0 \le r \le a \end{aligned} \tag{2.1}$$

$$\begin{aligned} E_{z2} &= [A_{n2} Z_{n2}(k_2 r) + A_{n3} Z_{n3}](k_2 r)] P_n \quad a \le r \le b \\ H_{z2} &= [B_{n2} Z_{n2}(k_2 r) + B_{n3} Z_{n3}](k_2 r)] Q_n \quad a \le r \le b \end{aligned} \tag{2.2}$$

$$\begin{aligned} E_{z3} &= A_{n4} Z_{n4}(k_3 r) P_n \quad b \le r \\ H_{z3} &= B_{n4} Z_{n4}(k_3 r) Q_n \quad b \le r \end{aligned} \tag{2.3}$$

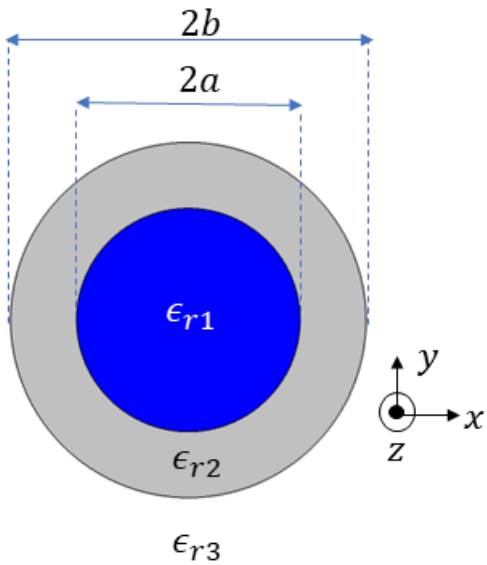

Figure 2.1: The 2D dielectric rod structure

where $P_n = \cos(n\phi)\exp(-j\beta z)$ and $Q_n = \sin(n\phi)\exp(-j\beta z)$. The parameter n determines the first mode number and $k_i, \quad i = 1-3$ is the wavenumber in the radial direction. The functions $Z_{nj}, \quad j = 1-4$ are Bessel and modified Bessel functions. The modes in this structure are classified based on where they start to attenuate in the radial direction into two groups. First, the cladding modes are the modes that are only being attenuated outside the cladding. The second type of mode is the core mode where the wave attenuation starts right after the boundary between the core and the cladding. To have a field attenuating in layer i, k_i should be imaginary. Another way of formulating the fields is to keep all the equations and variables real and choose the appropriate function based on where we want the mode to be attenuated. Having all real variables makes upcoming computations easier. The always real k_i is defined as follows[56]:

$$(k_i)^2 = k_0^2 v_i(\epsilon_{ri}\mu_{ri} - \bar{\beta}^2) \tag{2.4}$$

where $k_0 = \omega\sqrt{\epsilon_0\mu_0}$ is the wave number in vacuum. Parameter v_i is a variable

to keep k_i real and is defined as follows:

$$v_i = \begin{cases} 1, & \mu_{ri}\epsilon_{ri} \geq \bar{\beta}^2 \\ -1, & \mu_{ri}\epsilon_{ri} \leq \bar{\beta}^2 \end{cases} \tag{2.5}$$

where $\bar{\beta} = \frac{\beta}{k_0}$ and $i = 1 - 3$. The equality condition in the definition of v_i is not important as in this case $k_i = 0$. The choice of Z_{nj} in the above equations determines the type of the mode. For the cladding modes $v_1 = v_2 = 1 \quad \text{and} \quad v_3 = -1$. For these modes $\sqrt{\epsilon_{r3}} \leq \bar{\beta} \leq \sqrt{\epsilon_{r2}}$ considering $\mu_i = 1$ for all layers. For the core modes $v_1 = 1$ and $v_2 = v_3 = -1$. For these modes we have $\sqrt{\epsilon_{r2}} \leq \bar{\beta} \leq \sqrt{\epsilon_{r1}}$. From Maxwell's equations, The r and ϕ components can be found. According to the boundary conditions, the tangential component of the electric and magnetic field should be continuous at the boundaries. The continuity of $E_z, \quad H_z, \quad E_\phi$ and H_ϕ at $r = a$ gives 4 equations. The same field components should be continuous at $r = b$ which also provides 4 equations. These 8 equations alongside the 8 unknowns $(A_{nj}, B_{nj} \quad j = 1-4)$ make an 8 by 8 homogeneous linear system of equations.

$$D_{8\times8}C_{8\times1} = 0 \tag{2.6}$$

where $D_{8\times8}$ is defined as follows:

$$D_{8\times8} = \begin{bmatrix} Z_{n1}(k_1a) & 0 & -Z_{n2}(k_2a) & -Z_{n3}(k_2a) & \dots \\ 0 & Z_{n1}(k_1a) & 0 & 0 & \dots \\ \frac{n}{ak_1^2}\beta Z_{n1}(k_1a) & \frac{\omega\mu_0}{k_1}Z'_{n1}(k_1a) & \frac{n}{ak_2^2}\beta Z_{n2}(k_2a) & \frac{n}{ak_2^2}\beta Z_{n3}(k_2a) & \dots \\ \frac{\omega\epsilon_0\epsilon_{r1}}{k_1}Z'_{n1}(k_1a) & \frac{n}{ak_1^2}\beta Z_{n1}(k_1a) & \frac{\omega\epsilon_0\epsilon_{r2}}{k_2}Z'_{n2}(k_2a) & \frac{\omega\epsilon_0\epsilon_{r2}}{k_2}Z'_{n3}(k_2a) & \dots \\ 0 & 0 & Z_{n2}(k_2b) & Z_{n3}(k_2b) & \dots \\ 0 & 0 & 0 & 0 & \dots \\ 0 & 0 & -\frac{n}{bk_2^2}\beta Z_{n2}(k_2a) & -\frac{n}{bk_2^2}\beta Z_{n3}(k_2b) & \dots \\ 0 & 0 & \frac{\omega\epsilon_0\epsilon_{r2}}{k_2}Z'_{n2}(k_2b) & \frac{\omega\epsilon_0\epsilon_{r2}}{k_2}Z'_{n3}(k_2b) & \dots \end{bmatrix}$$

$$\begin{bmatrix} \dots & 0 & 0 & 0 & 0 \\ \dots & -Z_{n2}(k_2a) & -Z_{n3}(k_2a) & 0 & 0 \\ \dots & \frac{\omega\mu_0}{k_2}Z'_{n2}(k_2a) & \frac{\omega\mu_0}{k_2}Z'_{n3}(k_2a) & 0 & 0 \\ \dots & \frac{n}{ak_2^2}\beta Z_{n2}(k_2a) & \frac{n}{ak_2^2}\beta Z_{n3}(k_2a) & 0 & 0 \\ \dots & 0 & 0 & -Z_{n4}(k_3b) & 0 \\ \dots & Z_{n2}(k_2b) & Z_{n3}(k_2b) & 0 & -Z_{n4}(k_3b) \\ \dots & -\frac{\omega\mu_0}{k_2}Z'_{n2}(k_2b) & -\frac{\omega\mu_0}{k_2}Z'_{n3}(k_2b) & \frac{n}{bk_3^2}\beta Z_{n4}(k_3b) & \frac{\omega\mu_0}{k_3}Z'_{n4}(k_3b) \\ \dots & \frac{n}{bk_2^2}\beta Z_{n2}(k_2b) & \frac{n}{bk_2^2}\beta Z_{n3}(k_2b) & -\frac{\omega\epsilon_0\epsilon_{r3}}{k_3}Z'_{n4}(k_3b) & -\frac{n}{bk_3^2}\beta Z_{n4}(k_3b) \end{bmatrix} \tag{2.7}$$

Where $(Z_{nj})' = \frac{\partial}{\partial(k_i r)}(Z_{nj})$. Definition of the function Z_{nj} is given in the table below [56]:

Table 2.1: Definition of the function Z_{nj}

	Z_{n1}		Z_{n2}		Z_{n3}		Z_{n4}
IF	v_1=1	v_1=-1	v_2=1	v_2=-1	v_2=1	v_2=-1	v_3=-1
=	J_n	I_n	J_n	I_n	Y_n	K_n	K_n

Where J_n and Y_n are the Bessel function of the first and second kinds respectively. I_n and K_n are the modified Bessel function of the first and second kind respectively. The appropriate function should be picked based on the type of mode (cladding or core) that is determined by the values for v_1 and v_2. The only nontrivial solution to this system of equations can be obtained by setting the determinant of $D_{8\times8}$ equal to zero.

$$\det(D_{8\times8}) = F(\beta) = 0. \tag{2.8}$$

This equation is called the characteristics equation of the structure. Solving the characteristic equation for β yields the dispersion curves of the structure which show the variations of β versus a, the core radius, or frequency. The solution to this equation is explained in detail in paper A.

In order to find the fields' coefficients $C_{8\times1}$, equation (2.8) should first be solved for β. As the determinant of the $D_{8\times8}$ is zero, then the the rank of $D_{8\times8}$ is less than 8 and solving 2.6 is the same as finding the Null Space of $D_{8\times8}$ [58]. There are several ways to find the Null Space of a matrix. One way is to find the normalized coefficients [59]. The first coefficient, A_{n1} is set

to 1 and the other coefficients are found normalized to that. if $A_{n1} = 1$ then the first column of $D_{8\times8}$ is named $H_{8\times1}$ and the rest of the columns form matrix $D'_{8\times7}$. Then the remaining seven coefficients, $G_{7\times1}$ can be found by solving the following equation:

$$D'_{8\times7}G_{7\times1} \quad = \quad -H_{8\times1} \tag{2.9}$$

This equation is solved for $G_{1\times7}$ using the function `mldivide` in MATLAB R2020B which finds the solution that satisfies the leas-square error condition [60]. Then, the full coefficient's matrix is:

$$C_{8\times1} \quad = \quad [1, G^T_{7\times1}]^T. \tag{2.10}$$

Another method to find the null space is by using Singular Value Decomposition (SVD) which results in the same coefficients as the normalization method.

With the coefficients calculated, the normalized field components for any given mode at every location in space can be obtained. The normalized amplitudes of the z-component $|E_z|$ of HE_{11} and (TM_{01}, are plotted in Fig. 2.2. The two vertical dashed lines from left to right show the boundary of the core and cladding respectively. It can be seen that while the cladding mode (TM_{01} at 700 MHz) exhibits an ascending behavior in the cladding and then gets attenuated outside, for the core modes (The other three curves shown in Fig .2.2) the attenuation starts right after the boundary between the core and cladding. This means that the core modes are more confined inside the core, rather than outside it. Therefore, from the confinement point of view, it is more desirable to have a rod with a larger radius. The choice of the radius is investigated in paper A, part II by calculating the Normalized Modal Radius (NMR).

2D Numerical Simulations

To verify the accuracy of the solution presented earlier, the wave propagation problem in this structure is studied by using a 2D numerical solver. This solver is also used to design a Mode Suppressor that is added to the structure to prevent the excitation of the higher-order modes. The Modal analysis study for Electromagnetic Waves Frequency (ewfd) in COMSOL Multiphysics 5.6 is

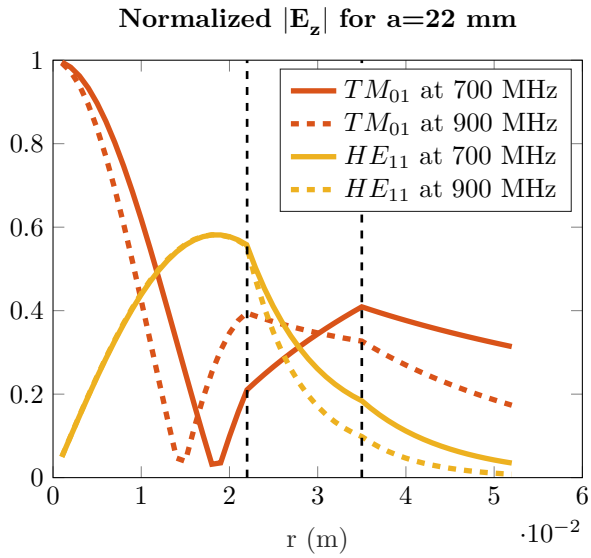

Figure 2.2: Normalized z-component of the electric field for four modes (two core and two cladding modes) at 2 frequencies

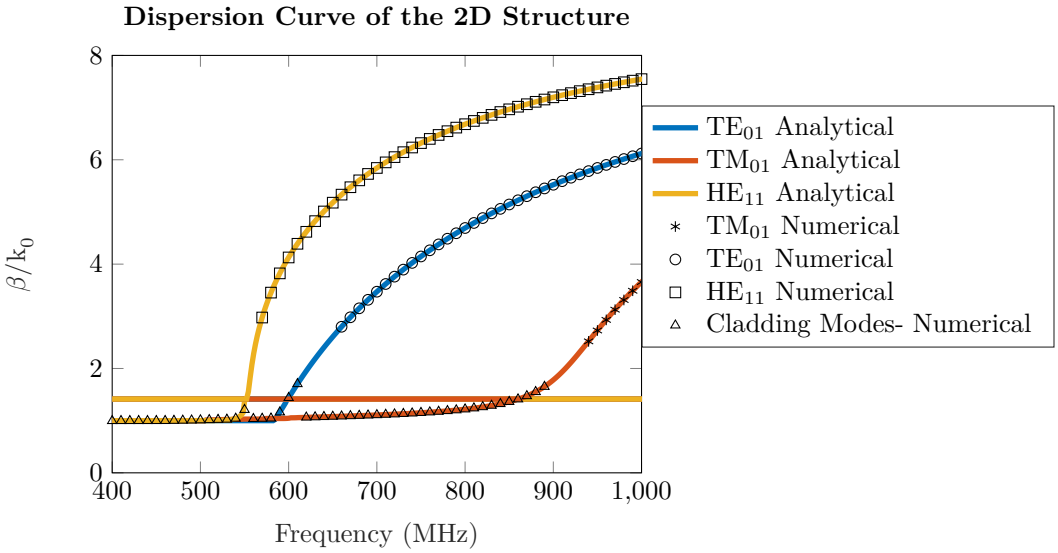

Figure 2.3: Comparison between the Analytical and the Numerical Solutions

used. For the core and cladding modes, two different simulations were run. For the former, the solver finds $\bar{\beta}$, around $\sqrt{\epsilon_{r1}}$ while for the latter the search for $\bar{\beta}$ is done around $\sqrt{\epsilon_{r2}}$. In Fig. 2.3, the analytical and numerical dispersion curves are compared with each other. The cladding mode simulation returns only a single propagating mode but as can be seen in this figure, it is in fact three different modes at different frequencies. A good agreement is seen between the analytical solution and simulation for the core modes at frequencies higher than the cut-off of the core modes which is the frequency where the cladding mode of a type turns into the core mode of the same type. Around these frequencies, some gaps are seen in the numerical dispersion curves.

The magnitude of the electric field for these three modes at a frequency where they are cladding (540 MHz for HE_{11} and 600 MHz for the other two) and core (900 MHz for all) are shown in Fig. 2.4. In each figure, the cladding and the core mode are shown in the left and right images respectively. Each mode is normalized to its maximum value. The arrows show the direction of

the tangential component of the field. From this figure, it can be seen that all of the modes become more confined inside the rod as the mode turns into a core mode.

2.2 Launching Efficiency of the 2D Modes in the 3D Structure

In this section, we investigate how much of the input power is guided through each of the modes. To show quantitatively how much the higher order modes TE_{01} and TM_{01} are excited, the method introduced in paper B can be used. The fields excited on a DRA can be written as follows [61]:

$$E^{3D} = \sum_{p=1}^{m} A_p E_p^{2D} + E_R \tag{2.11}$$

Where E^{3D} is the total 3D field, E_p^{2D} is a 2D guided wave mode, m is the number of the propagating modes, and E_R is the radiating field, i.e. has an imaginary k_3. The unknown of this equation, A_p can be obtained by applying the orthogonality of the guided fields to each other and the radiating field [61]:

$$\int (E_p^{2D} \times H_q^{2D}) \cdot \hat{z} da = 0 \; for \; p \neq q. \tag{2.12}$$

$$\int (E_R \times H_q^{2D}) \cdot \hat{z} da = 0. \tag{2.13}$$

Combining (2.11)-(2.13), the coefficient of each mode can be found as:

$$A_p = \frac{\int (E^{3D} \times H_p^{2D}) \cdot \hat{z} da}{\int (E_p^{2D} \times H_p^{2D}) \cdot \hat{z} da}. \tag{2.14}$$

An important figure of merit for guided modes is the Launching Efficiency. It can be calculated for a single mode or the summation of the modes and is defined as follows [62]:

$$\alpha_p = \frac{\frac{1}{2} \int (\Re(\hat{E_p}^{3D} \times \hat{H_p}^{3D^*})) \cdot \hat{z} da}{P_{in}} \tag{2.15}$$

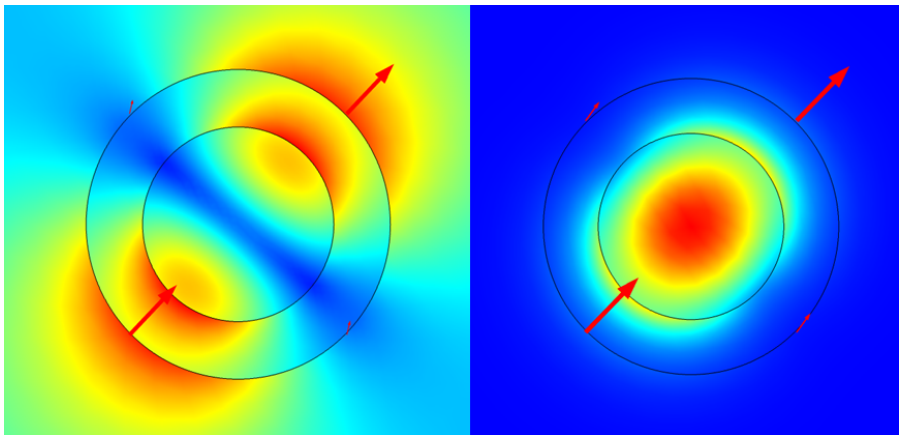

(a) HE_{11} mode

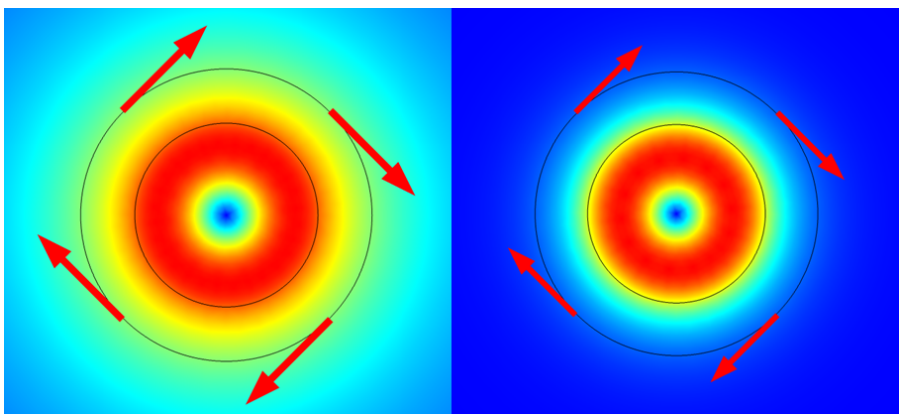

(b) TE_{01} mode

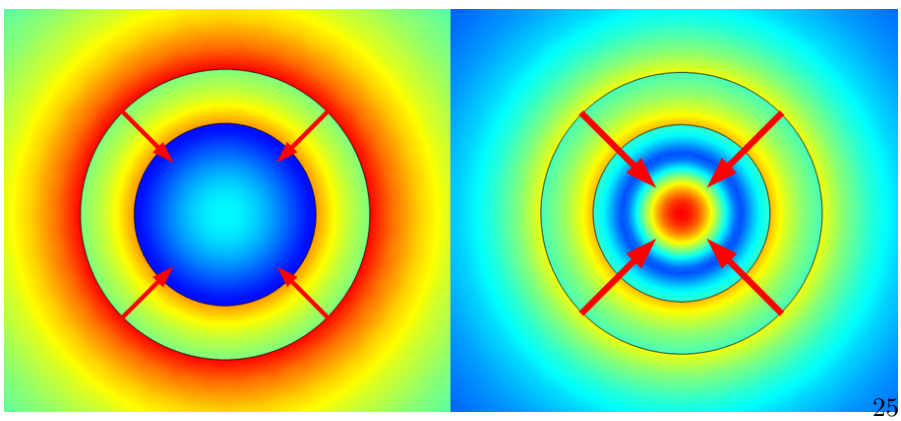

(c) TM_{01} mode

Figure 2.4: The magnitude of the 2D simulated electric fields when they are a cladding (left) and a core (right) mode. The arrows show the direction of the tangential component of the field.

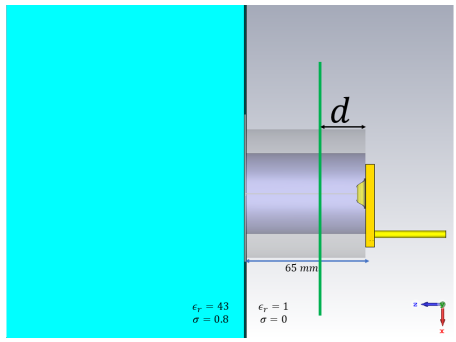

Figure 2.5: The 3D simulated DRA, the sampling plane is shown with a green line. The Sampling plane is in distance d from the start point of the DRA

Where $*$ shows the complex conjugate operation, $\hat{E_p}^{3D} = A_p E_p^{2D}$ and $\hat{H_p}^{3D^*}$ are the approximated 3D electric and magnetic fields of each mode respectively. P_{in} shows the total power entered into the exciter. Here, it had been set to the value of the accepted power in the waveguide port in the 3D simulation to eliminate the effect of the variation in the performance of the exciter at different frequencies. The launching efficiency, α_p of each mode are shown in Fig. 2.6 versus different distances from the start point of the DRA shown by d in Fig. 2.5. As seen in this Fig. 2.6, The efficiency of the excitation of the fundamental mode, HE_{11} is considerably higher than that of the two higher order modes and it is maintained along the rod. Therefore, the power that is coupled to the higher-order modes is small. To improve this, a mode suppressor is designed in paper A, to prevent the excitation of TE_{01}.

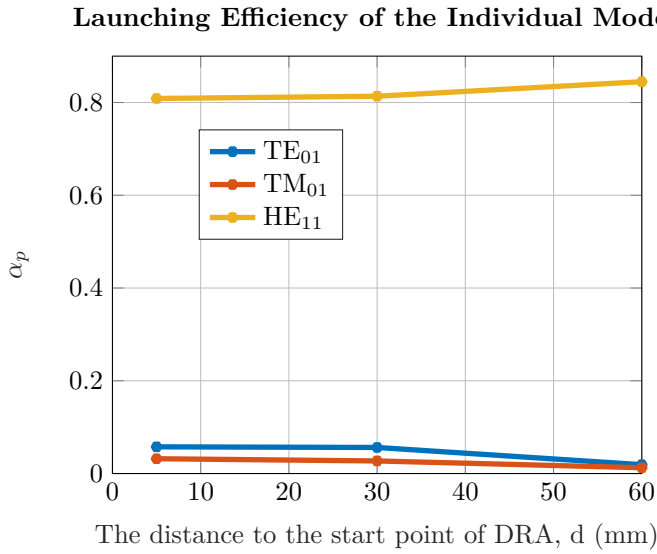

Figure 2.6: Launching efficiency of each mode versus the distance of the sampling plane to the start point of the DRA, d.

CHAPTER 3

Animal Study

In this chapter, the aim and summary, of an ongoing study on animals are presented. Some preliminary results of applying an anomaly detection algorithm on previously measured data are also presented.

3.1 The Necessity and Conditions of the Animal Study

As discussed in chapter 1, microwave diagnosis of stroke is a challenge. Since the thrombus does not introduce a significant change in the distribution of the permittivity in the brain, its effect on the EM wave is subtle. This subtle change is hard to detect given the noise and other limitations of the measurements. One solution to this challenge is to use antennas with lower susceptibility to interference and microwave transceivers with high Signal to Noise Ratio (SNR). Possible solutions for improving the antennas was discussed in chapter 2. The challenges and solutions for improved SNR will be discussed in the next section. Another way to increase the accuracy of the measurements is the introduction of a Contrast-Enhancing Agent (CEA). As mentioned in

chapter 1, with CEA, the difference between the permittivity of the part of the brain that the CEA reaches and the part that it doesn't reach increases. As this is an invasive method that has not been tested on humans before, it needs to be verified in an animal study first.

For this purpose, we have chosen a sheep model. Sheep have the advantage that the head is relatively similar to the human head. The animal study is performed at the SEARCH laboratory of the Faculty of Veterinary Medicine, Norwegian University of Life Sciences, Sandnes, Norway. In what follows, the regulations on the use of animals in research is reviewed.

The Use of Animals in Research

In Norway, the use of laboratory animals is governed by the Regulation concerning the use of animals for scientific purposes (FOR-2015-06-18-761) [63]. Based on those regulations, a set of ethical guidelines is given by the National Committee for Research Ethics in Science and Technology (NENT) [64]. According to the guideline, the ethical grounds for the moral duties regarding the animals come from the following three positions:

- Animals have intrinsic value which must be respected.
- Animals are sentient creatures with the capacity to feel pain, and the interest of animals must be taken into consideration.
- Our treatment of animals is an expression of our attitudes as moral actors.

This guideline defines 10 responsibilities and requirements for the researchers to use animals in the research. Among them, the three starting with R (Replace, Reduce and Refine) are emphasized as the other 7 are based on them. These three Rs are:

- **Replace**: Researchers need to do their best to find ways to replace animals with other methods for their research. In this research, the first step is to simulate the detection system in a computer simulation environment and test the system in the lab on phantoms. But in the end, as the detection method depends on the blood circulation system using animals is inevitable.

- **Reduce**: The number of animals used in the research should be reduced as much as possible. In the case of clarity of success or failure of the project in the early stages, the experiments on animals should be stopped and no more animals shall suffer.
- **Refine**: Researchers are responsible to minimize the risk of suffering of the animals. In this project, most of the work concerning the state of the animal is administered by veterinarians. As they are experts in working with animals, they have more authority than engineers. What an engineer can do is to make the system more comfortable for the animal and make the measurement process faster so the animal suffers less although it is sedated.

The animal study is planned and performed following these regulations and guidelines.

3.2 The Plan for the Animal Study

In this section, the ongoing setup forthe animal study is explained.

Contrast-Enhancing Agent

In this study, we investigate the possibility of using saline. It has been shown that the injection of saline into in-vitro samples of canine blood can change the permittivity and conductivity [65]. Saline solutions are cost-efficient and easily accessible. Additionally, administering hypertonic saline solutions to stroke patients is an approved treatment in emergency medicine [66]. The volume and dosage of the injected saline solution and the speed of injection are the factors that play role in the detection accuracy and are to be investigated in the animal study.

Numerical Simulations

In this section, the results of a numerical simulation as a proof of concept for the idea of enhancing the contrast by injecting a conductive solution are presented. The simulations are done using CST Microwave Studio 2020. The simulation setup is shown in Fig. 3.1. Six Antennas are placed around the numerical model of the sheep. The simulation is done once for the baseline

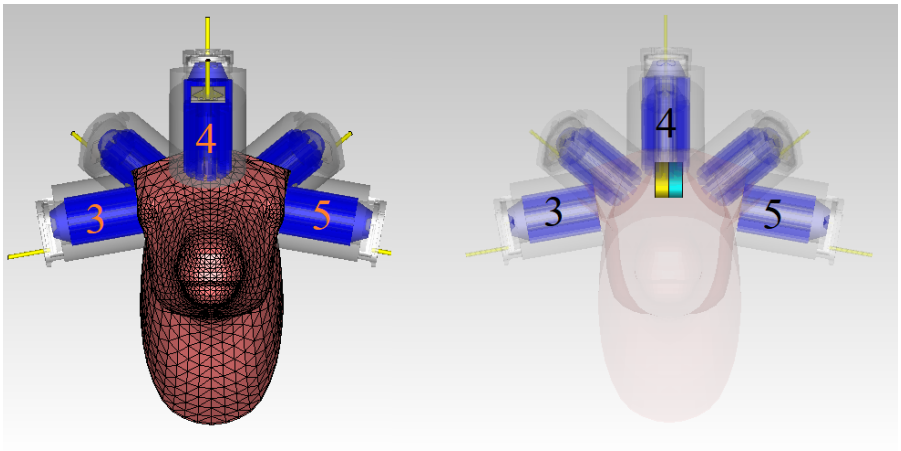

Figure 3.1: Baseline Simulation (left) and the Injection Simulation (right). The left lobe of the brain (shown in yellow) has different dielectric properties than the right lobe.

measurement and once for the injection measurement when the permittivity and conductivity of the left lobe of the brain are changed and are lossier. The transmission coefficient for these two simulations and the difference made by the injection in the transmission coefficient are shown in Fig. 3.2. The difference is shown by the subtraction of the baseline simulated coefficients from their corresponding coefficients in the injection simulation. As seen in Fig. 3.2, the change in the transmission coefficient in the lobe where the permittivity and conductivity have changed is stronger than that of the right lobe.

Measurement Hardware

The long-term goal of the study is to develop a fast and portable device to support the decision-making process in pre-hospital stroke detection when an ambulance arrives at a patient. Therefore, the microwave transceiver should be compact and portable. In this research, two devices are tested.

- Keysight N7081A Microwave Transceiver is a compact 2-port Vector Network Analyzer that has a high measurement speed in a wide range of

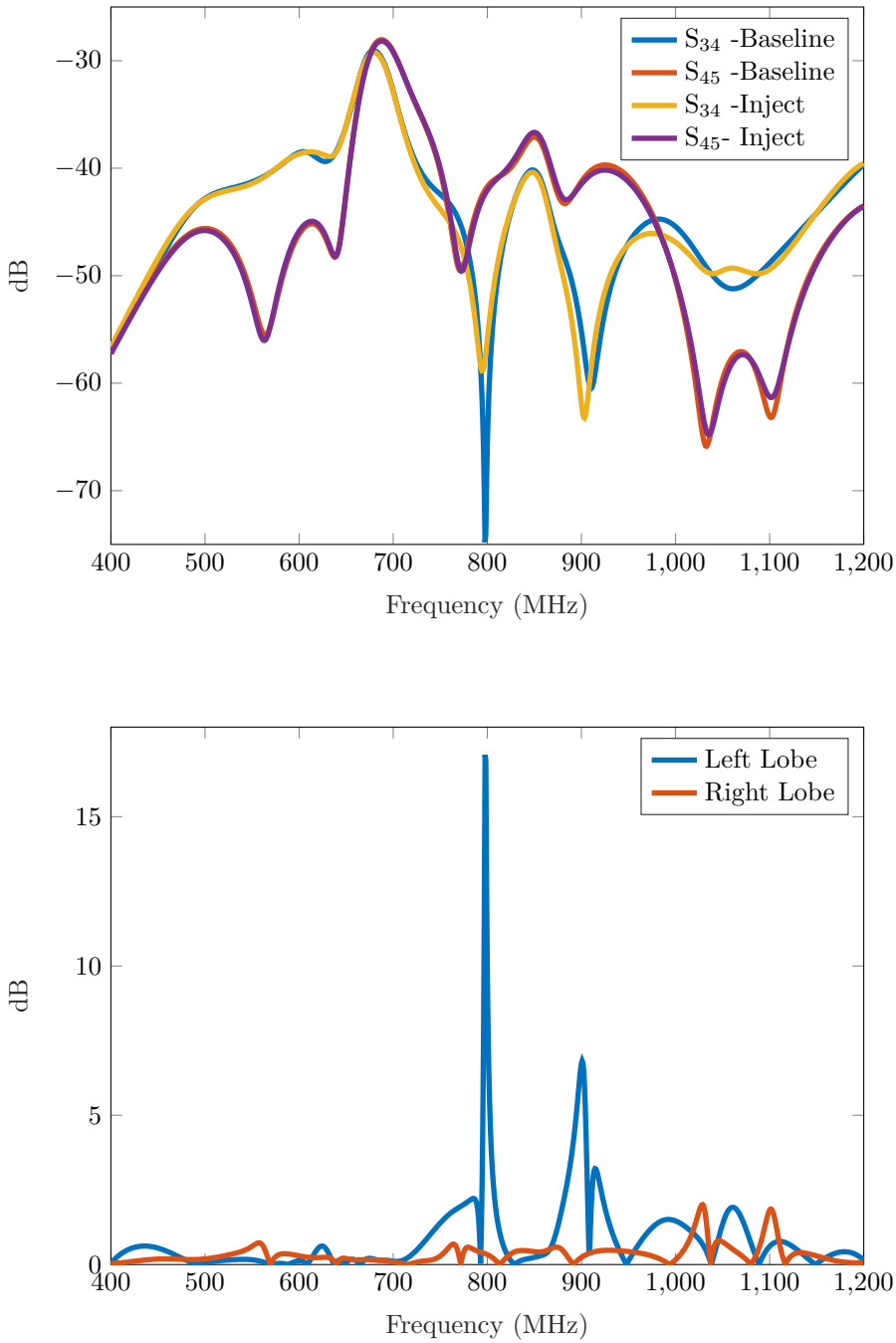

Figure 3.2: The Transmission Coefficient in the left and right lobe, before and after the injection (top) and subtraction of the baseline from the injection in the left and right lobe (bottom)

Figure 3.3: N7981A (left) and USRP-2920 (right)

frequencies and is a pulsed system. based on Pseudo-random sequences.

- National Instrument USRP-2920 Software Define Radio (SDR) is a tunable single frequency RF transceiver with a high-speed analog-to-digital converter and digital-to-analog converter.

Both systems had been used before in microwave biomedical diagnostics [67], [68] and are shown in Fig. 3.3. In Table 3.1, a comparison between the specifications of these two devices is made [69], [70].

In table 3.1, the specifications of the two devices and the settings used in this study are compared. The dynamic range of N7081, depends on the number of hardware and software averaging. A higher number of averaging results in a higher dynamic range but slows down the measurement. The 70 dB dynamic range stated in the table is with 100 hardware averaging. This can potentially be increased to 105 dB if both hardware and software averaging are used. The measurement time in table 3.1 shows the time of sweeping 200 frequency points. For SDR, another limiting factor is the time that it needs to save the received packet of data before sending the next one. Not allowing enough time for this might result in measurement failure.

	N7081A	USRP-2920
Frequency Range	100 KHz to 5 GHz	50 MHz to 2.2 GHz
Dynamic Range	70 dB	80 dB
Frequency accuracy	±5 ppm	±2.5 ppm
Measurement Time	0.8 s	5.6 s

Table 3.1: Comparison between the Specifications and Settings of Transceivers

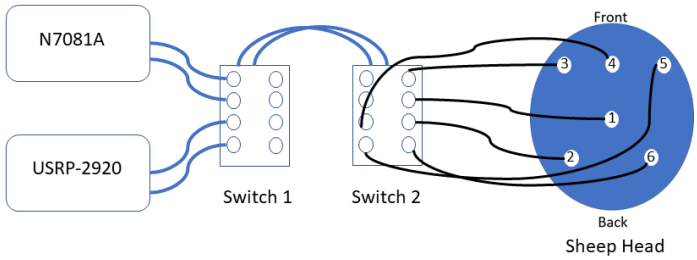

Figure 3.4: The Schematic of the Measurement System and the Configuration of the Antenna (white circles) on the Sheep Head

Two DP8T Solid State Switch Modules from RANAtech are used [71]. The first switch changes the transceiver and the second one switches between the antennas. Each switch introduces around 6 dB attenuation to the system.

A full measurement is when both of the two microwave transceivers have swept all the frequency range and $n-1$ antennas have transmitted the signal if n is the total number of the antennas. The switching between the receiver antenna is done as follows. When antenna number i is the transmitter, the receiver port should be switched between antenna number $i+1$ to n. In total $\frac{n(n-1)}{2}$ transmission coefficients will be measured. The other $\frac{n(n-1)}{2}$ transmission coefficients are the same due to reciprocity. These $n(n-1)$ transmission alongside n reflection coefficients, create a full $n \times n$ scattering matrix. The schematic of the measurement system is shown in Fig. 3.4.

Measurement Protocol

The procedure for the previous animal experiment was according to the following protocol. First, the animal is sedated and fixed on the bed. The heartbeat and the blood pressure of the animal are measured continuously. The antennas are placed on the sheep's head as shown in Fig. 3.5. Then, the Baseline measurement starts. Following that, the three-stage measurement begins and is repeated several times. The stages are:

- **Stroke**: A balloon had been inserted into one of the arteries of the animal before the baseline measurement starts. In this stage, the balloon is inflated to block the blood circulation in that artery and act as an

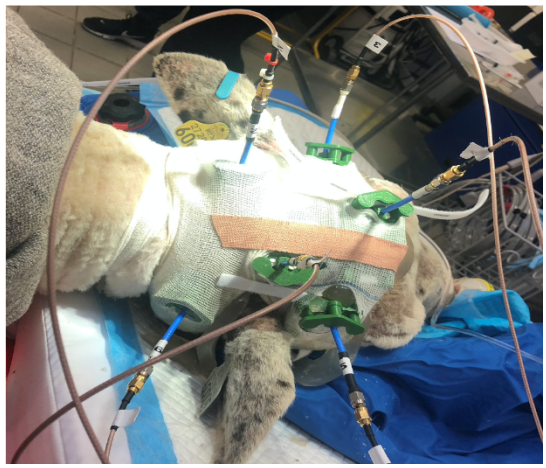

Figure 3.5: The Antenna Placement on the Sheep Head

induced stroke. Then, the signals are measured in this stage.

- **Injection** The CEA is injected into one of the veins of the animal. The signals are continuously being measured during this stage.
- **Opening** The artery becomes open again by deflating the balloon. The measurement is done after the artery opens up.

In each stage, 8-12 measurement instances are performed.

3.3 Preliminary Results of Anomaly Detection Algorithm

In this section, some preliminary results of applying an unsupervised anomaly detection algorithm on the previously measured data is presented. This algorithm follows the idea introduced in [34] and is based on the symmetry assumption between the left and right lobe of the brain. By calculating the distance Correlation (dCorr) between sets of transmitting channels, where one set is picked from the channels propagating through the left lobe and the other through the right lobe, the change due to anomaly is detectable.

If $X = [x_1, ..., x_p]^T$ and $Y = [y_1, ..., y_q]^T$ are two data vectors of p and q dimensions respectively, and $X^{(1)}, ..., X^{(n)}$ and $Y^{(1)}, ..., Y^{(n)}$ are two N independent and identically distributed (i.i.d) random realizations of X and Y, then the dCorr is defined as [72]:

$$dC = \mathrm{dCorr}(X,Y) \quad = \begin{cases} \frac{v_N^2(X,Y)}{\sqrt{v_N^2(X)v_N^2(Y)}} & v_N^2(X)v_N^2(Y) > 0 \\ 0 & v_N^2(X)v_N^2(Y) = 0 \end{cases} \tag{3.1}$$

where

$$\begin{aligned} v_N^2(X,Y) &= \frac{1}{N^2}\sum_{k,l=1}^{N} A_{kl}B_{kl} \\ A_{kl} &= a_{kl} - \bar{a_{k.}} - \bar{a_{.l}} + \bar{a_{..}} \\ B_{kl} &= b_{kl} - \bar{b_{k.}} - \bar{b_{.l}} + \bar{b_{..}} \end{aligned} \tag{3.2}$$

with $a_{kl} = ||X^{(k)} - X^{(l)}||$, $b_{kl} = ||Y^{(k)} - Y^{(l)}||$ and

$$\begin{aligned} \bar{a_{k.}} = \frac{1}{N}\sum_{l=1}^{N} a_{kl}, \quad \bar{a_{.l}} = \frac{1}{N}\sum_{k=1}^{N} a_{kl}, \quad \bar{a_{..}} = \frac{1}{N^2}\sum_{k,l=1}^{N} a_{kl} \\ \bar{b_{k.}} = \frac{1}{N}\sum_{l=1}^{N} b_{kl}, \quad \bar{b_{.l}} = \frac{1}{N}\sum_{k=1}^{N} b_{kl}, \quad \bar{b_{..}} = \frac{1}{N^2}\sum_{k,l=1}^{N} b_{kl} \end{aligned} \tag{3.3}$$

When dC between the two signals approaches 1, it means that the two signals are similar to each other. A $dC = 0$ translates to the statistical independence between X and Y. The two important feature of the dCorr is that first it reveals the non-linear relation between the two signal X and Y and second, they can be of different dimensions.

In the anomaly detection algorithm, each of X and Y are a single s-parameter or a group of s-parameters. For instance $X = S_{21}$ and $Y = S_{31}$ or $X = [S_{21}, S_{41}]$ and $Y = [S_{31}, S_{51}, S_{71}]$. Each of the $X^{(k)}$ and $Y^{(k)}$ is a sample of the s-parameter in frequency or time. For example, if the first frequency that is sent is 400 MHz, then $X^{(1)} = [S_{21}(400\mathrm{MHz}), S_{41}(400\mathrm{MHz})]$ according to the previous example.

The number and configuration of the antenna on the animal head are shown in Fig. 3.4. The dCorr value between each pair of transmission channels, one passing through the left lobe of the brain and the other one through the right

is calculated at different stages of the experiment and shown in Fig. 3.6. The signals used for calculating dCorr are filtered between 560 and 880 MHz. In this figure, B stands for Baseline, S for Stroke, I for injection, and O for Opening. The number after each letter shows the repetition number. In this experiment, the three stages were repeated three times. As Fig. 3.6 shows, a clear decrease (7%) in the similarity between the two signals received from the left and right lobe of the brain is observable at the moment of the first injection. This change is more visible between channels S_{13} and S_{15}.

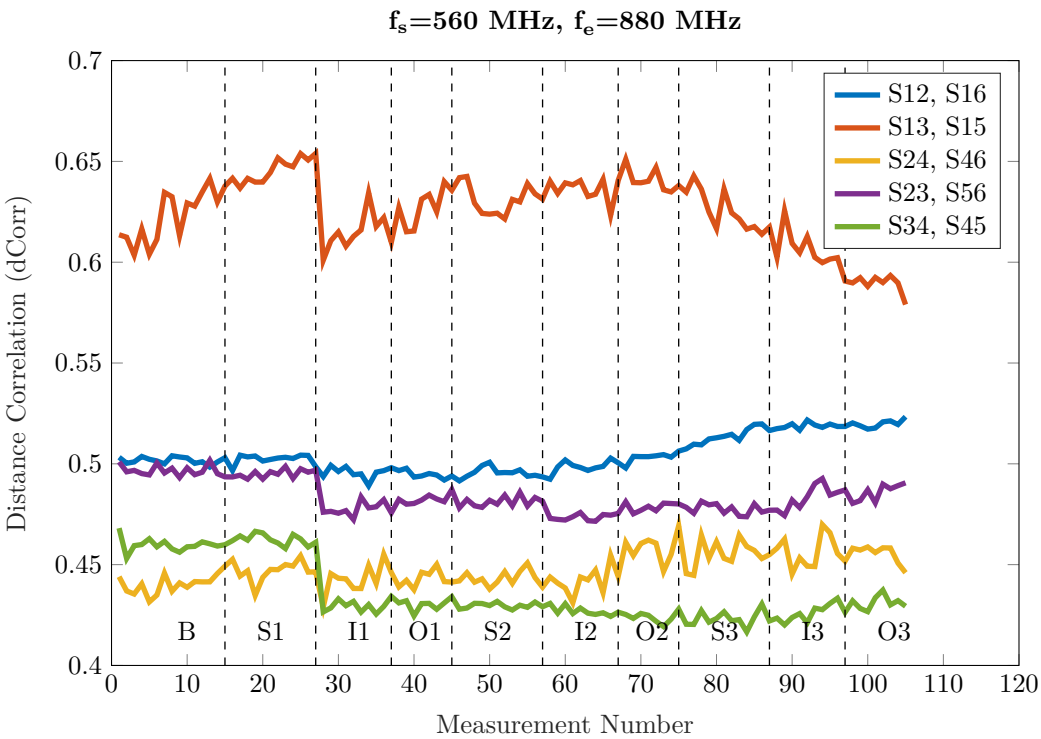

Figure 3.6: Distance correlation between different pairs of transmission coefficient. In each pair, one is transmission to the right and the other is to the left. The horizontal axis shows the measurement instance number

CHAPTER 4

Summary of included papers

This chapter provides a summary of the included papers.

4.1 Paper A

Seyed Moein Pishnamaz, Xuezhi Zeng, Hana Dobšíček Trefná, Mikael Persson, Andreas Fhager
Minimising the Surface Waves By Using a Dielectric Rod Antenna in Near-Field Biomedical Diagnostics
To be Submitted to IEEE Transactions on Antenna and Propagation.

In this paper, the problem of minimizing the surface waves on the surface of a tissue-mimicking phantom is investigated. It was shown that by moving a Self-Grounded Bow-Tie antenna at a distance from the surface of the body and placing a dielectric rod in between, the power on the surface is confined in the rod rather than propagating on the surface of the body. The rod is designed based on an analytical wave propagation method and modified by using of a 2D numerical solver to have a wide-single-core propagation bandwidth. The structure of the bow-tie antenna plus dielectric waveguide can be viewed as

a Dielectric Rod Antenna. The minimization of the surface power is shown numerically and the distance where most of the surface power is confined inside is found to be half for DRA in comparison with SGBTA. The power on the surface of the tank is reduced up to 10 dB in an experimental setup. The addition of the dielectric rod to the SGBTA results in a better matching to the phantom, in other words, widening the -10 dB bandwidth of the system. Besides, it gives a stable gain in a wide range of frequencies. The dimensions of the antenna are $0.26 \times 0.18\lambda_0$ at the center frequency and can be still considered as a compact antenna. Therefore, it can be used in a multi-antenna biomedical diagnosis system.

4.2 Paper B

Seyed Moein Pishanamz, Andreas Fhager, Mikael Persson
Analysis of the 2D Guided Mode Propagation in a 3D Dielectric Rod Antenna
Submitted to 17th European Conference on Antenna and Propagation.

This paper presents how the 2-dimensional guided mode propagation analysis relates to an analysis of a 3-dimensional dielectric rod antenna. An approximated model based on the summation of the guided modes multiplied by the coefficients obtained by projecting the 3D fields on the 2D fields is derived and the accuracy is investigated. The factors playing a role in the error of the approximation are studied and it is concluded that the main cause of error in the guided mode propagation approximation is the reflection from the truncation at the end of the rod rather than the radiating field along the rod.

CHAPTER 5

Conclusion and Future Work

In this thesis background and results of our work on the diagnostics of thromboses in the brain, using microwave technology were presented. The aim of this ongoing project is to develop a diagnostic device that is able to identify thrombectomy candidates so that this group of patients will, to a higher degree, be transported to thrombectomy centers faster than today.

In this thesis, the design and development of an antenna that creates fewer surface waves around the body were presented. The antenna was designed to deliver sufficient power to the body with a high gain and a low return loss. This was achieved by placing a dielectric rod in front of the radiating element and converting the original Self Grounded Bow-Tie Antenna (SGBTA) to a dielectric rod antenna (DRA). It was shown that with this design the power of the surface waves decreases up to 10 dB compared with the SGBTA. It was also shown that the DRA design had a considerably more stable gain throughout the frequency window of operation as well as a 72% increase in the bandwidth compared to the previous design.

The microwave transceivers that are used for the animal study were introduced and compared. Simulation results were presented as proof in preparation for the upcoming animal study. Preliminary results from using an

anomaly detection algorithm on data from performed measurements on sheep were also presented. The results were quite encouraging.

The next step in this research project is to develop an array of the designed antennas and test them on the phantom and animal models. The data will then be analyzed using the anomaly detection algorithm which will also be developed further as the project progresses. Another challenge that needs to be addressed is the measurement speed. As the time that it takes for the CEA to reach the brain is short, the detection device should be able to perform fast measurements to capture the effect of CEA injection. In the next step of the project, we will therefore evaluate the performance of the two microwave transceivers with the aim of minimizing the measurement speed while maintaining the accuracy level.

References

[1] A. Ingeman, "Medical complications in patients with stroke: Data validity, processes of care, and clinical outcome," Ph.D. dissertation, Aarhus University, Aarhus, Denmark, 2010.

[2] V. L. Feigin, B. A. Stark, C. O. Johnson, *et al.*, "Global, regional, and national burden of stroke and its risk factors, 1990–2019: A systematic analysis for the global burden of disease study 2019," *The Lancet Neurology*, vol. 20, no. 10, pp. 795–820, 2021.

[3] R. Lozano, M. Naghavi, K. Foreman, *et al.*, "Global and regional mortality from 235 causes of death for 20 age groups in 1990 and 2010: A systematic analysis for the global burden of disease study 2010," *The lancet*, vol. 380, no. 9859, pp. 2095–2128, 2012.

[4] C. J. Murray, T. Vos, R. Lozano, *et al.*, "Disability-adjusted life years (dalys) for 291 diseases and injuries in 21 regions, 1990–2010: A systematic analysis for the global burden of disease study 2010," *The lancet*, vol. 380, no. 9859, pp. 2197–2223, 2012.

[5] V. L. Feigin, G. A. Roth, M. Naghavi, *et al.*, "Global burden of stroke and risk factors in 188 countries, during 1990–2013: A systematic analysis for the global burden of disease study 2013," *The Lancet Neurology*, vol. 15, no. 9, pp. 913–924, 2016.

[6] J. Olesen, A. Gustavsson, M. Svensson, *et al.*, "The economic cost of brain disorders in europe," *European journal of neurology*, vol. 19, no. 1, pp. 155–162, 2012.

[7] B. H. Johnson, M. M. Bonafede, and C. Watson, "Short-and longer-term health-care resource utilization and costs associated with acute ischemic stroke," *ClinicoEconomics and outcomes research: CEOR*, vol. 8, p. 53, 2016.

[8] J. M. Wardlaw, V. Murray, E. Berge, and G. J. Del Zoppo, "Thrombolysis for acute ischaemic stroke," *Cochrane database of systematic reviews*, no. 7, 2014.

[9] M. Palaniswami and B. Yan, "Mechanical thrombectomy is now the gold standard for acute ischemic stroke: Implications for routine clinical practice," *Interventional neurology*, vol. 4, no. 1-2, pp. 18–29, 2015.

[10] W. Hacke, M. Kaste, E. Bluhmki, *et al.*, "Thrombolysis with alteplase 3 to 4.5 hours after acute ischemic stroke," *New England journal of medicine*, vol. 359, no. 13, pp. 1317–1329, 2008.

[11] J. Thunman, B. Södergård, N. Eckard, C. Nilsson, and S. Hiort, "Hälsoekonomisk utvärdering av trombektomi för behandling av akut svår ischemisk stroke," *Kunskapsunderlag. Stockholm: Tandvårds-och läkemedelsförmånsverket*, 2015.

[12] M. Persson, A. Fhager, H. D. Trefná, *et al.*, "Microwave-based stroke diagnosis making global prehospital thrombolytic treatment possible," *IEEE Transactions on Biomedical Engineering*, vol. 61, no. 11, pp. 2806–2817, 2014.

[13] I. C. Odland, S. Chennareddy, R. Kalagara, *et al.*, "Prehospital stroke detection devices: A bibliometric analysis of current trends," *World Neurosurgery*, vol. 167, e1360–e1375, 2022.

[14] A. Kiourti, A. M. Abbosh, M. Athanasiou, *et al.*, "Next-generation healthcare: Enabling technologies for emerging bioelectromagnetics applications," *IEEE Open Journal of Antennas and Propagation*, vol. 3, pp. 363–390, 2022.

[15] R. Hood, M. Persson, A. Fhager, *et al.*, "Evaluating the sensitivity and specificity of a microwave based tool to support and enhance stroke triage," in *INTERNATIONAL JOURNAL OF STROKE*, SAGE PUBLICATIONS LTD 1 OLIVERS YARD, 55 CITY ROAD, LONDON EC1Y 1SP, ENGLAND, vol. 17, 2022, pp. 64–65.

[16] K. B. Walsh, "Non-invasive sensor technology for prehospital stroke diagnosis: Current status and future directions," *International Journal of Stroke*, vol. 14, no. 6, pp. 592–602, 2019.

[17] L. Yang, W. Liu, R. Chen, *et al.*, "In vivo bioimpedance spectroscopy characterization of healthy, hemorrhagic and ischemic rabbit brain within 10 hz–1 mhz," *Sensors*, vol. 17, no. 4, p. 791, 2017.

[18] T. Scheeren, P. Schober, and L. Schwarte, "Monitoring tissue oxygenation by near infrared spectroscopy (nirs): Background and current applications," *Journal of clinical monitoring and computing*, vol. 26, no. 4, pp. 279–287, 2012.

[19] L. di Biase, A. Bonura, M. L. Caminiti, P. M. Pecoraro, and V. Di Lazzaro, "Neurophysiology tools to lower the stroke onset to treatment time during the golden hour: Microwaves, bioelectrical impedance and near infrared spectroscopy," *Annals of Medicine*, vol. 54, no. 1, pp. 2658–2671, 2022.

[20] J. C. Maxwell, *A treatise on electricity and magnetism*. Clarendon press, 1873, vol. 1.

[21] A. Vander Vorst, A. Rosen, and Y. Kotsuka, *RF/microwave interaction with biological tissues*. John Wiley & Sons, 2006.

[22] *Electromagnetic spectrum*
, `https://sites.google.com/site/tmbssciencehomeworkmrr/electromagnetic-spectrum`, Accessed: 2022-12-09.

[23] D. M. Pozar, *Microwave engineering*. John wiley & sons, 2011.

[24] P. M. Meaney, M. W. Fanning, D. Li, S. P. Poplack, and K. D. Paulsen, "A clinical prototype for active microwave imaging of the breast," *IEEE Transactions on Microwave Theory and Techniques*, vol. 48, no. 11, pp. 1841–1853, 2000.

[25] S. Hosseinzadegan, A. Fhager, M. Persson, S. D. Geimer, and P. M. Meaney, "Discrete dipole approximation-based microwave tomography for fast breast cancer imaging," *IEEE Transactions on Microwave Theory and Techniques*, vol. 69, no. 5, pp. 2741–2752, 2021.

[26] V. Mattsson, L. L. Ackermans, B. Mandal, *et al.*, "Mas: Standalone microwave resonator to assess muscle quality," *Sensors*, vol. 21, no. 16, p. 5485, 2021.

[27] L. Guerrero Orozco, L. Peterson, and A. Fhager, "Microwave antenna system for muscle rupture imaging with a lossy gel to reduce multipath interference," *Sensors*, vol. 22, no. 11, p. 4121, 2022.

[28] A. S. Janani, S. A. Rezaeieh, A. Darvazehban, M. Khosravi-Farsani, S. E. Keating, and A. M. Abbosh, "Electromagnetic method for steatotic liver detection using contrast in effective dispersive permittivity," *IEEE Journal of Electromagnetics, RF and Microwaves in Medicine and Biology*, 2022.

[29] D. Ireland and M. Bialkowski, "Microwave head imaging for stroke detection," *Progress In Electromagnetics Research M*, vol. 21, pp. 163–175, 2011.

[30] A. Fhager, S. Candefjord, M. Elam, and M. Persson, "Microwave diagnostics ahead: Saving time and the lives of trauma and stroke patients," *IEEE Microwave Magazine*, vol. 19, no. 3, pp. 78–90, 2018.

[31] A. Fhager, S. Candefjord, M. Elam, and M. Persson, "3d simulations of intracerebral hemorrhage detection using broadband microwave technology," *Sensors*, vol. 19, no. 16, p. 3482, 2019.

[32] M. Hopfer, R. Planas, A. Hamidipour, T. Henriksson, and S. Semenov, "Electromagnetic tomography for detection, differentiation, and monitoring of brain stroke: A virtual data and human head phantom study.," *IEEE Antennas and Propagation Magazine*, vol. 59, no. 5, pp. 86–97, 2017.

[33] J. A. Tobon Vasquez, R. Scapaticci, G. Turvani, *et al.*, "A prototype microwave system for 3d brain stroke imaging," *Sensors*, vol. 20, no. 9, p. 2607, 2020.

[34] A. Brankovic, A. Zamani, A. Trakic, *et al.*, "Unsupervised algorithm for brain anomalies localization in electromagnetic imaging," *IEEE Transactions on Computational Imaging*, vol. 6, pp. 1595–1606, 2020.

[35] *Medfield diagnostics ab*, `https://www.medfielddiagnostics.com/`.

[36] S. Semenov, T. Huynh, T. Williams, B. Nicholson, and A. Vasilenko, "Dielectric properties of brain tissue at 1 ghz in acute ischemic stroke: Experimental study on swine.," *Bioelectromagnetics*, vol. 38, no. 2, pp. 158–163, 2016.

[37] D. O. Rodriguez-Duarte, J. A. T. Vasquez, R. Scapaticci, L. Crocco, and F. Vipiana, "Assessing a microwave imaging system for brain stroke monitoring via high fidelity numerical modelling," *IEEE Journal of Electromagnetics, RF and Microwaves in Medicine and Biology*, vol. 5, no. 3, pp. 238–245, 2021.

[38] R. Scapaticci, O. Bucci, I. Catapano, and L. Crocco, "Differential microwave imaging for brain stroke followup," *International Journal of Antennas and Propagation*, vol. 2014, 2014.

[39] D. Carr, J. Brown, G. Bydder, *et al.*, "Gadolinium-dtpa as a contrast agent in mri: Initial clinical experience in 20 patients," *American Journal of Roentgenology*, vol. 143, no. 2, pp. 215–224, 1984.

[40] J. S. Hudson, T. K. Chung, B. S. Prout, Y. Nagahama, M. L. Raghavan, and D. M. Hasan, "Iron nanoparticle contrast enhanced microwave imaging for emergent stroke: A pilot study," *Journal of Clinical Neuroscience*, vol. 59, pp. 284–290, 2019.

[41] R. Lahri, M. Rahman, M. Wright, P. Kosmas, and M. Thanou, "Zinc oxide nanoparticles as contrast-enhancing agents for microwave imaging," *Medical physics*, vol. 45, no. 8, pp. 3820–3830, 2018.

[42] S. Coşğun, E. Bilgin, and M. Çayören, "Microwave imaging of breast cancer with factorization method: Spions as contrast agent," *Medical Physics*, vol. 47, no. 7, pp. 3113–3122, 2020.

[43] A. Madannejad, J. EbrahimiZadeh, F. Ravanbakhsh, M. D. Perez, and R. Augustine, "Reflectometry enhancement by saline injection in microwave-based skin burn injury diagnosis," in *2020 14th European Conference on Antennas and Propagation (EuCAP)*, IEEE, 2020, pp. 1–4.

[44] G. Van Rhoon, P. Rietveld, and J. Van der Zee, "A 433 mhz lucite cone waveguide applicator for superficial hyperthermia," *International journal of hyperthermia*, vol. 14, no. 1, pp. 13–27, 1998.

[45] P. Togni, Z. Rijnen, W. Numan, *et al.*, "Electromagnetic redesign of the hypercollar applicator: Toward improved deep local head-and-neck hyperthermia," *Physics in Medicine & Biology*, vol. 58, no. 17, p. 5997, 2013.

[46] P. Takook, M. Persson, J. Gellermann, and H. D. Trefná, "Compact self-grounded bow-tie antenna design for an uwb phased-array hyperthermia applicator," *International Journal of Hyperthermia*, vol. 33, no. 4, pp. 387–400, 2017.

[47] M. Ghaderi Aram, H. Aliakbarian, and H. Dobšıček Trefná, "An ultra-wideband compact design for hyperthermia: Open ridged-waveguide antenna," *IET Microwaves, Antennas & Propagation*, vol. 16, no. 2-3, pp. 137–152, 2022.

[48] T. Alves, B. Poussot, and J.-M. Laheurte, "Analytical propagation modeling of ban channels based on the creeping-wave theory," *IEEE Transactions on Antennas and Propagation*, vol. 59, no. 4, pp. 1269–1274, 2010.

[49] P. M. Meaney, F. Shubitidze, M. W. Fanning, M. Kmiec, N. R. Epstein, and K. D. Paulsen, "Surface wave multipath signals in near-field microwave imaging," *International journal of biomedical imaging*, vol. 2012, 2012.

[50] X. Li, *Body matched antennas for microwave medical applications*. KIT Scientific Publishing, 2014, vol. 72.

[51] U. Rafique, S. Pisa, R. Cicchetti, O. Testa, and M. Cavagnaro, "Ultra-wideband antennas for biomedical imaging applications: A survey," *Sensors*, vol. 22, no. 9, p. 3230, 2022.

[52] M. Rokunuzzaman, A. Ahmed, T. C. Baum, and W. S. Rowe, "Compact 3-d antenna for medical diagnosis of the human head," *IEEE Transactions on Antennas and Propagation*, vol. 67, no. 8, pp. 5093–5103, 2019.

[53] H. Chen and K.-M. Luk, "An on-body matched differentially fed magnetoelectric dipole antenna for head imaging systems," *IEEE Transactions on Antennas and Propagation*, vol. 70, no. 11, pp. 10 032–10 046, 2022.

[54] H. Dobšıček Trefná, J. Vrba, and M. Persson, "Evaluation of a patch antenna applicator for time reversal hyperthemia," *International Journal of Hyperthermia*, vol. 26, no. 2, pp. 185–197, 2010.

[55] R. Kazemi, A. E. Fathy, and R. A. Sadeghzadeh, "Dielectric rod antenna array with substrate integrated waveguide planar feed network for wideband applications," *IEEE Transactions on Antennas and Propagation*, vol. 60, no. 3, pp. 1312–1319, 2012.

[56] A. Safaai-Jazi and G. Yip, "Classification of hybrid modes in cylindrical dielectric optical waveguides," *Radio Science*, vol. 12, no. 4, pp. 603–609, 1977.

[57] C. A. Balanis, *Advanced engineering electromagnetics*. John Wiley & Sons, 2012.

[58] G. Strang, G. Strang, G. Strang, and G. Strang, *Introduction to linear algebra*. Wellesley-Cambridge Press Wellesley, MA, 1993, vol. 3.

[59] K. Y. Kim, H.-S. Tae, J.-H. Lee, and H.-S. Kim, "Analysis of dielectric loss in three-region all dielectric circular waveguides," *KIEE International Transactions on Electrophysics and Applications*, vol. 12, no. 3, pp. 181–185, 2002.

[60] Mathworks, *Mldivide*, `https://se.mathworks.com/help/matlab/ref/mldivide.html`, Accessed: 2022-12-09.

[61] A. Snyder, "Surface waveguide modes along a semi-infinite dielectric fiber excited by a plane wave," *JOSA*, vol. 56, no. 5, pp. 601–606, 1966.

[62] G. Yip, "Launching of the he11 surface-wave mode on a dielectric rod," *Electronics Letters*, vol. 6, no. 1, pp. 2–3, 1970.

[63] *Regulations on the use of animals in experiments*, `https://lovdata.no/dokument/SF/forskrift/2015-06-18-761`.

[64] *Ethical guidelines for the use of animals in research*, `https://www.forskningsetikk.no/en/guidelines/science-and-technology/ethical-guidelines-for-the-use-of-animals-in-research/`.

[65] E. D. Trutman and R. S. Newbower, "A practical analysis of the electrical conductivity of blood," *IEEE Transactions on Biomedical Engineering*, no. 3, pp. 141–154, 1983.

[66] J. Bardutzky and S. Schwab, "Antiedema therapy in ischemic stroke," *Stroke*, vol. 38, no. 11, pp. 3084–3094, 2007.

[67] A. T. Mobashsher, A. M. Abbosh, and Y. Wang, "Microwave system to detect traumatic brain injuries using compact unidirectional antenna and wideband transceiver with verification on realistic head phantom," *IEEE Transactions on Microwave Theory and Techniques*, vol. 62, no. 9, pp. 1826–1836, 2014.

[68] X. Zeng and L. G. Orozco, "Measurement quality of a software defined radio system for medical diagnostics," *The Journal of Engineering*, 2022.

[69] Keysight, *N7081a microwave transceiver*, https://www.keysight.com/se/en/assets/9018-04678/technical-specifications/9018-04678.pdf.

[70] NI, *Usrp-2920 specifications*, https://www.ni.com/docs/en-US/bundle/usrp-2920-specs/page/specs.html#GUID-0CAFCB88-62D1-4128-B786-23D00B72BCFE__GUID-C1B8A6E6-A258-48FA-B67E-6A0306024209.

[71] Ranatech, *Ri 2582 solid state switch*, https://ranatec.com/wp-content/uploads/2021/12/Datasheet-RI-2582-rev.-E.pdf.

[72] G. J. Székely, M. L. Rizzo, and N. K. Bakirov, "Measuring and testing dependence by correlation of distances," *The annals of statistics*, vol. 35, no. 6, pp. 2769–2794, 2007.